

Thin-film periodically poled lithium niobate waveguides fabricated by femtosecond laser photolithography

GUANGHUI ZHAO,^{1,4} JINTIAN LIN,^{1,5,6,12} RENHONG GAO,^{2,3,11} JIANGLIN GUAN,^{2,3} CHUNTAO LI,^{2,3} XINZHI ZHENG,^{2,3} MINGHUI LI,^{1,5} QIFENG HOU,^{1,6} XIAOCHAO LUO,^{1,5} YINGNUO QIU,^{1,5} LINGLING QIAO,¹ MIN WANG,² AND YA CHENG^{1,2,3,4,7,8,9,10,13}

¹State Key Laboratory of Ultra-intense Laser Science and Technology, Shanghai Institute of Optics and Fine Mechanics (SIOM), Chinese Academy of Sciences (CAS), Shanghai 201800, China

²The Extreme Optoelectromechanics Laboratory (XXL), School of Physics and Electronic Science, East China Normal University, Shanghai 200241, China

³State Key Laboratory of Precision Spectroscopy, East China Normal University, Shanghai 200062, China

⁴School of Physical Science and Technology, ShanghaiTech University, Shanghai 200031, China

⁵Center of Materials Science and Optoelectronics Engineering, University of Chinese Academy of Sciences, Beijing 100049, China

⁶School of Physical Sciences, University of Science and Technology of China, Hefei 230026, China

⁷Shanghai Research Center for Quantum Sciences, Shanghai 201315, China

⁸Hefei National Laboratory, Hefei 230088, China

⁹Collaborative Innovation Center of Extreme Optics, Shanxi University, Taiyuan 030006, China

¹⁰Collaborative Innovation Center of Light Manipulations and Applications, Shandong Normal University, Jinan 250358, China

¹¹rhgao@phy.ecnu.edu.cn

¹²jintianlin@siom.ac.cn

¹³ya.cheng@siom.ac.cn

April 21, 2025

Periodically poled lithium niobate on insulator (PPLNOI) ridge waveguides are critical photonic components for both classical and quantum information processing. However, dry etching of PPLNOI waveguides often generates rough sidewalls and variations in the etching rates of oppositely poled lithium niobate ferroelectric domains, leading a relatively high propagation losses (0.25–1 dB/cm), which significantly limits net conversion efficiency and hinders scalable photonic integration. In this work, a low-loss PPLNOI ridge waveguide with a length of 7 mm was fabricated using ultra-smooth sidewalls through photolithography-assisted chemo-mechanical etching followed by high-voltage pulse poling. The average surface roughness was measured at just 0.27 nm, resulting in significantly lower propagation loss compared to dry-etched counterparts. Highly efficient second-harmonic generation was demonstrated with a normalized efficiency of 1,742% $W^{-1}\cdot\text{cm}^{-2}$ and an overall efficiency of 750.1%/W (without accounting for propagation loss). The absolute conversion efficiency reached 15.8%, representing a six-fold improvement over the best previously reported values in single-period PPLNOI waveguides without magnesium oxide doping.

In recent years, the commercialization of thin-film lithium niobate on insulator (LNOI) wafers and advancements in ultra-low-loss waveguide fabrication technologies [1,2] have established LNOI as a highly promising material platform for multi-functional integrated

photonics [3-5]. This is attributed to the strong optical confinement combined with the superior optical properties of LNOI, including low material loss, broad transparency window, strong electro-optic effect, and significant second-order nonlinear optical responses. Leveraging these advantages, various photonic devices such as high-speed electro-optic modulators, efficient nonlinear frequency converters, and entangled photon pair sources have been demonstrated on LNOI platforms [1-5,6-11]. Among these applications, nonlinear integrated photonic devices based on ferroelectric domain engineering have garnered significant interest for both classical and quantum information processing [12-23]. As a typical ferroelectric material, lithium niobate (LN) allows post-fabrication domain inversion through poling processes, enabling quasi-phase matching (QPM) to significantly enhance nonlinear conversion efficiency via periodic poling.

The fabrication of PPLNOI waveguides involves two essential processes: ferroelectric domain inversion and waveguide etching. These can be performed in sequence [13-16,18-23] or inversely [17,24,25]. However, periodically poled lithium niobate (PPLN) exhibits selective anisotropic etching issues during reactive ion etching and other processes like RCA cleaning [24]. The accessible nonlinear conversion efficiency is highly susceptible to propagation loss, necessitating low propagation loss for high conversion efficiency. Conventional fabrication procedures involving periodic domain inversion followed by waveguide etching result in

significant propagation losses (~ 1 dB/cm) in the telecom band, severely limiting net conversion efficiency and scalability.

To address this challenge, an alternative approach involves performing periodic poling after waveguide etching. This method only introduces a slight additional propagation loss (from 0.23 dB/cm to 0.25 dB/cm in the telecom band before and after periodic poling [24]). The primary cause of this propagation loss is the relatively rough sidewall of dry-etched waveguides, with an average surface roughness of ~ 1 nm. To further improve net conversion efficiency and enable large-scale scalable photonic integration, it is essential to fabricate PPLNOI waveguides with ultra-smooth sidewalls to reduce propagation losses.

In this work, a low propagation-loss PPLNOI ridge waveguide (7 mm long) was fabricated via femtosecond laser photolithography-assisted chemo-mechanical etching (PLACE) followed by periodic poling. This method avoids sidewall morphology degradation and periodic parameter deviations caused by anisotropic etching in conventional methods. The resulting PPLNOI ridge waveguide features ultra-smooth surfaces and sidewalls with an average surface roughness of 0.27 nm, significantly reducing scattering loss. Highly efficient second harmonic generation (SHG) was achieved, with a normalized conversion efficiency of $1,742\% \cdot W^{-1} \cdot cm^{-2}$, overall efficiency of $750.1\%/W$, and absolute conversion efficiency of 15.8% at room temperature (without deducting propagation loss). This technique offers a reliable pathway for large-scale, high-density nonlinear photonic circuits.

A commercially available X-cut LNOI wafer (Shanghai Novel Si Integration Technology Co.) was used in this experiment, which consists of a 500-nm-thick LN thin-film layer, a $4.7\text{-}\mu\text{m}$ -thick silicon dioxide (SiO_2) buffer layer and an LN handle. The PPLNOI ridge waveguide was fabricated by waveguide etching using PLCAE technique followed by periodic poling, as schematically illustrated in Figure 1. First, a 200-nm-thick chromium (Cr) layer was deposited on the thin-film lithium niobate (TFLN) via magnetron sputtering. Second, a femtosecond pulsed laser was used to selectively ablate the Cr layer for generating strip patterns with a width of $1\ \mu\text{m}$, oriented to Y axis of the crystal. Third, chemo-mechanical polishing (CMP) was employed to etch the exposed TFLN with a depth of 210 nm, resulting in pattern transferring from Cr mask pattern to the TFLN. The residual Cr mask was removed via wet etching after the fabrication of LNOI ridge waveguide. Fourth, a multilayer stack of 100 nm Cr, 200 nm Au, and 100 nm Ti was sequentially sputtered onto the pre-fabricated ridge waveguide sample to produce microelectrodes by lift-off process. Fifth, femtosecond laser direct writing was then used to pattern the Ti layer by ablation. Sixth, the Ti mask pattern was transferred to the Au layer via inductively coupled plasma reactive ion etching (ICP-RIE). Seventh, the exposed Cr and residual Ti were etched away by wet etching, leading to the fabrication of the comb-shaped Cr-Au electrodes. Eighth, to achieve domain inversion, several high-voltage pulses (400 V, 5 ms duration) were applied to the comb-shaped electrodes, generating periodic poling in the ridge waveguide region. The spacing between the electrode pair was approximately $7\ \mu\text{m}$, yielding an electric field strength of ~ 51.7 kV/mm, which exceeds the coercive field of bulk LN crystals (21 kV/mm), ensuring effective domain inversion. Finally, the residual Cr-Au electrodes were subsequently removed

via chemical etching, resulting in the fabrication of the PPLNOI ridge waveguides.

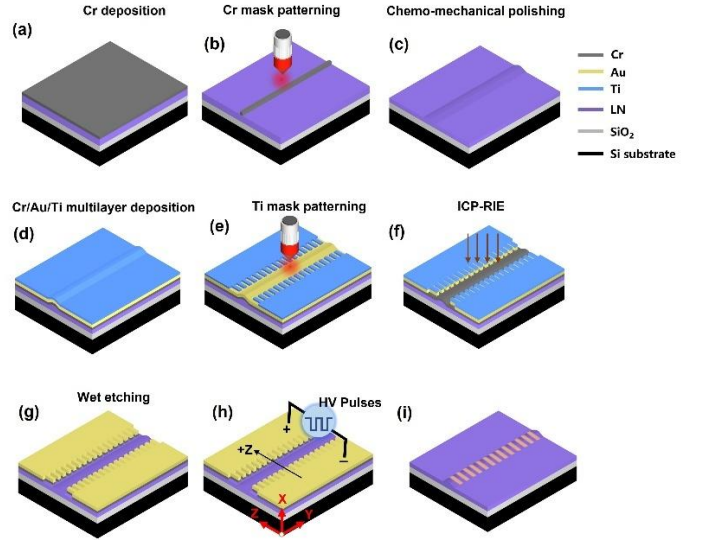


Fig. 1. Schematic of the fabrication the PPLNOI waveguide.

The optical microscope image of the fabricated PPLNOI ridge waveguide shows an ultra-smooth surface, as depicted in Fig. 2(a). And the scanning electron microscope (SEM) image of the cross section of ridge waveguide is shown in Fig. 2(b). The average surface roughness was measured to be only 0.27 nm by atomic force microscopy, as shown in the inset of Fig. 2(e). Consequently, low propagation loss on the order of magnitude of 0.027 dB/cm can be expected, thanks to the ultra-smooth sidewall [27] and the elimination of anisotropic etching of periodic poling microstructures [24]. Moreover, this ridge waveguide only supports single-mode guiding in the telecom band, which is very important for high efficiency SHG by maximizing the overlap integral between the fundamental and the second harmonic modes. Since the poling period Λ should provide optical momentum for quasi-phase matched SHG, it is necessary to calculate the effective refractive indices of the fundamental and the second harmonic modes. And the poling period was determined by the formula $\Lambda = \lambda_{2\omega} / (n_{2\omega} - n_{\omega})$. Here, $\lambda_{2\omega}$, $n_{2\omega}$, and n_{ω} are the wavelength of the second harmonic in vacuum, the refractive indices of the second harmonic and the pump modes, respectively. The transverse-electrically (TE) polarized modal profiles are simulated by the finite element analysis method, as depicted in Fig. 2(c). And the effective refractive indices of both the 1550-nm pump and its second-harmonic modes are calculated to 1.8656 and 2.0797, respectively. Figure 2(d) illustrates the calculated QPM period as a function of the pump wavelength. As the pump wavelength redshifts, the required poling period gradually increases. When the pump wavelength was set at 1550 nm, the corresponding poling period should be $3.62\ \mu\text{m}$. After the fabrication of the PPLNOI ridge waveguide, the ferroelectric domain inversion was non-destructively characterized using confocal second harmonic (SH) microscopy, as depicted in Fig. 2(e), where P_s labeled with a white line represents the spontaneous polarization orientation of LN. And the black line represents the domain inversion.

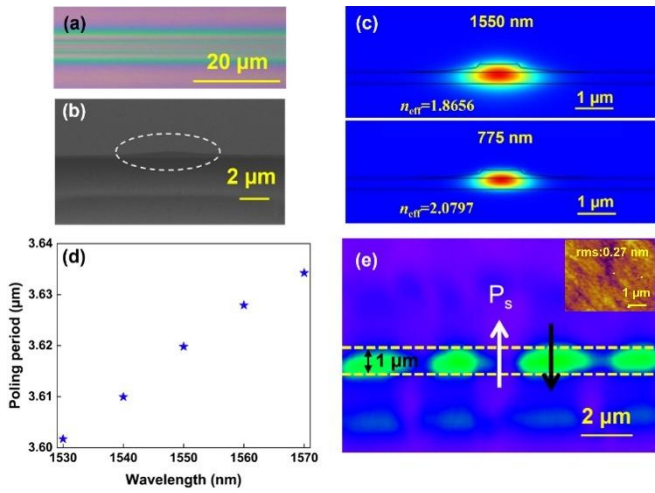


Fig. 2. Optical micrograph of the single-mode PPLNOI waveguide. (b) The SEM image of the cross section of the ridge waveguide. (c) Mode field profiles and effective refractive indices of the fundamental and second harmonic modes in the waveguide. (d) Simulation of optimum poling period varied with pump wavelengths. (e) Image of the domain inversion structure of the waveguide recorded using the confocal SH microscopy, where the waveguide was labeled with yellow lines with dashes. Inset: atomic force microscope (AFM) image of the waveguide.

To achieve SHG in the PPLNOI waveguide, a telecom-band tunable continuous-wave laser (Model: TLB-6728, New Focus Inc.) amplified with an erbium-doped fiber amplifier (EDFA) was employed as the pump source. The schematic of the experimental setup is shown in Figure 3. An inline fiber polarization controller was exploited to ensure the pump light was TE-polarized during the experiment. A lensed fiber was used for end-face coupling to inject pump light into the ridge waveguide. And an optical microscope imaging system which consists of an objective lens with numerical aperture of 0.25 and a charge coupled device (CCD) camera was mounted above the device under test (i.e., the waveguide chip, denoted as DUT) to monitor the coupling. Successively, the generated second harmonic signal was coupled out of the waveguide using another lensed fiber and sent to an optical spectrum analyzer (denoted as OSA, Model: YOKOGAWA AQ6370D) to monitor the second-harmonic signal and record its power. And the waveguide chip was placed on a thermoelectric heater for tuning the temperature. Here, the fiber-to-chip coupling losses of ~ 11 dB/facet and ~ 24 dB/facet have been calibrated and extracted by measuring the linear optical transmission at both pump and second harmonic wavelengths, respectively.

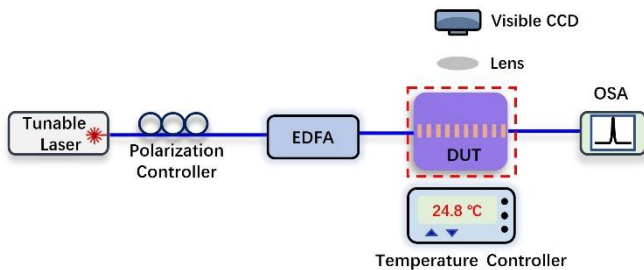


Fig. 3. Experimental setup for testing the PPLNOI waveguide.

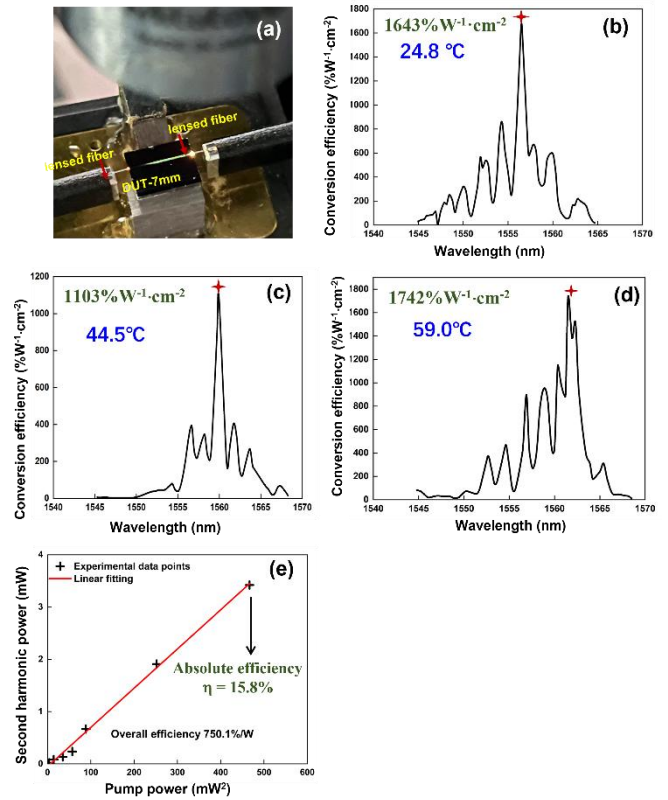


Fig. 4. Bright SHG generated in the waveguide captured by a smartphone. Normalized conversion efficiency of second harmonic as a function of pump wavelength at (b) 24.8°C, (c) 44.5°C, and (d) 59.0°C. (e) Quadratic power dependence of the second harmonic power on the pump power.

The pump wavelength was scanned from 1545 nm to 1565 nm, and the generated second harmonic signal was recorded by the OSA. When the temperature was set to room temperature (24.8°C), the normalized SHG conversion efficiency dependence on pump wavelength is plotted in Fig. 4(b). A highest normalized SHG conversion efficiency was measured as $1643 \text{ \%W}^{-1}\cdot\text{cm}^{-2}$ at 1556.56 nm pump. And bright SHG is visible to the naked eye, which was captured with a camera of a smart mobile phone, as shown in Fig. 4(a). Moreover, to improve the conversion efficiency, it is necessary to perform temperature tuning of the PPLNOI waveguide to improve phase match using the temperature heater. Typical experimental data was shown in Figs. 4(c) and 4(d), which were measured at 44.5°C and 59°C, respectively. The optimal phase-matching wavelength exhibited a red-shift with increasing temperature, corresponding to 1559.85 nm at 44.5°C and 1561.51 nm at 59°C. And the normalized conversion efficiencies were measured to $1103 \text{ \%W}^{-1}\cdot\text{cm}^{-2}$, and $1742 \text{ \%W}^{-1}\cdot\text{cm}^{-2}$, respectively. Furthermore, the output power of second harmonic varied with pump powers was measured at 1561.51 nm pump. Figure 4(e) illustrates a linear relationship between the SHG output power and the square of the pump light, yielding an overall SHG conversion efficiency of $750.1 \text{ \%}/\text{W}$ without deducting the propagation loss. The absolute SHG conversion efficiency reaches a maximum of 15.8% (calculated according to the formula $\eta_{SHG} = P_{SHG}/P_{FW}$ where P_{SHG} and P_{FW} represent second harmonic and pump powers,

respectively) at a pump level of 21.6 mW, corresponding to 3.4 mW SHG output. This absolute conversion efficiency surpasses the previously reported values achieved in single-period PPLNOI waveguides without doping with magnesium oxide [19], representing ~ six-fold improvement.

In this work, a 7-mm-long low-loss PPLNOI waveguides has been fabricated by waveguide etching and microelectrode poling using the PLCAE technique to achieve efficient quasi-phase-matched SHG. Thanks to the ultra-smooth sidewalls of the waveguides produced by chemo-mechanical polishing and the elimination of anisotropic etching of PPLNOI waveguides in conventional fabrication processes, high normalized conversion efficiency, absolute conversion efficiency, and overall conversion efficiency have been demonstrated as $1,742\% \cdot W^{-1} \cdot cm^{-2}$, 15.8%, and $750.1\%W^{-1}$, respectively. Since the PLCAE technique allows large-scale photonic integration with low propagation loss [27], our work opens up new opportunities for future quantum and classical photonic applications.

Acknowledgment. We thank Dr. Lei Yang of East China Normal University for helping us to acquire the image of the domain inversion structure of the waveguide.

References

1. J. Lin, F. Bo, Y. Cheng, and J. Xu. Advances in on-chip photonic devices based on lithium niobate on insulator[J]. *Photon. Res.*, **8**, 1910-1936 (2020).
2. Y. Jia, L. Wang, and F. Chen. Ion-cut lithium niobate on insulator technology: Recent advances and perspectives[J]. *Appl. Phys. Rev.*, **8**, 011307 (2021).
3. G. Chen, N. Li, J. Ng, H. Lin, Y. Zhou, Y. Fu, L. Lee, Y. Yu, A. Liu, and A. Danner. Advances in lithium niobate photonics: development status and perspectives[J]. *Adv. Photonics*, **4**, 034003 (2022).
4. Z. Xie, F. Bo, J. Lin, H. Hu, X. Cai, X.-H. Tian, Z. Fang, J. Chen, M. Wang, F. g Chen, Y. Cheng, J. Xu, and S. Zhu. Recent development in integrated lithium niobate photonics[J]. *Adv. Phys. X*, **9**, 2322739 (2024).
5. Y. Zheng and X. Chen. Nonlinear wave mixing in lithium niobate thin film[J]. *Adv. Phys. X*, **6**, 1889402 (2020).
6. J. Lin, N. Yao, Z. Hao, J. Zhang, W. Mao, M. Wang, W. Chu, R. Wu, Z. Fang, L. Qiao, W. Fang, F. Bo, and Y. Cheng. Broadband quasi-phase-matched harmonic generation in an on-chip monocrystalline lithium niobate microdisk resonator[J]. *Phys. Rev. Lett.* **122**, 173903 (2019).
7. M. Li, L. Chang, L. Wu, J. Staffa, J. Ling, U. A. Javid, S. Xue, Y. He, R. Lopez-rios, T. J. Morin, H. Wang, B. Shen, S. Zeng, L. Zhu, K. J. Vahala, J. E. Bowers, and Q. Lin. Integrated Pockels laser[J]. *Nat. Commun.* **13**, 5344 (2022).
8. C. Wang, M. Zhang, X. Chen, M. Bertrand, A. Shams-Ansari, S. Chandrasekhar, P. Winzer, and M. Lončar. Integrated lithium niobate electro-optic modulators operating at CMOS-compatible voltages[J]. *Nature*, **562**, 101-104 (2018).
9. B. Fu, R. Gao, N. Yao, H. Zhang, C. Li, J. Lin, M. Wang, L. Qiao, and Y. Cheng. Soliton microcomb generation by cavity polygon modes[J]. *Opto-Electronic Adv.* **7**, 240061 (2024).
10. J. Ma, F. Xie, W. Chen, J. Chen, W. Wu, W. Liu, Y. Chen, W. Cai, M. Ren, and J. Xu. Nonlinear lithium niobate metasurfaces for second harmonic generation[J]. *Laser Photon. Rev.* **15**, 2000521 (2021).
11. R. Bao, Z. Fang, J. Liu, Z. Liu, J. Chen, M. Wang, R. Wu, H. Zhang, and Y. Cheng. An Erbium-doped waveguide amplifier on thin film lithium niobate with an output power exceeding 100 mW[J]. *Laser Photon. Rev.* **19**, 2400765 [2024].
12. H. Jin, F. M. Liu, P. Xu, J. L. Xia, M. L. Zhong, Y. Yuan, J.W. Zhou, Y. X. Gong, W. Wang, and S. N. Zhu. On-chip generation and manipulation of entangled photons based on reconfigurable lithium-niobate waveguide circuits[J]. *Phys. Rev. Lett.* **113**, 103601 (2014).
13. X. Wang, X. Jiao, B. Wang, Y. Liu, X.-P. Xie, M.-Y. Zheng, Q. Zhang, and J.-W. Pan. Quantum frequency conversion and single-photon detection with lithium niobate nanophotonic chips[J]. *npj Quantum Information* **9**, 38 (2023).
14. J. Zhao, C. Ma, M. Rusing, and S. Mookherjee. High quality entangled photon pair generation in periodically poled thin-film lithium niobate waveguides[J]. *Phys. Rev. Lett.*, **124**, 163603 (2020).
15. G.-T. Xue, Y.-F. Niu, X. Liu, J.-C. Duan, W. Chen, Y. Pan, K. Jia, X. Wang, H.-Y. Liu, Y. Zhang, P. Xu, G. Zhao, X. Cai, Y.-X. Gong, X. Hu, Z. Xie, and S. Zhu. Ultrabright multiplexed energy-time-entangled photon generation from lithium niobate on insulator chip[J]. *Phys. Rev. Appl.* **15**, 064059 (2021).
16. Z. Hao, L. Zhang, W. Mao, A. Gao, X. Gao, F. Gao, F. Bo, G. Zhang, and J. Xu. Second-harmonic generation using d_{33} in periodically poled lithium niobate microdisk resonators[J]. *Photon. Res.* **8**, 311-317 (2020).
17. J. Lu, M. Li, C.-L. Zou, A. A. Sayem, and H. X. Tang. Toward 1% single-photon anharmonicity with periodically poled lithium niobate microring resonators[J]. *Optica*, **7**, 1654-1659 (2020).
18. X. Wu, L. Zhang, Z. Hao, R. Zhang, R. Ma, F. Bo, G. Zhang, and J. Xu. Broadband second-harmonic generation in step-chirped periodically poled lithium niobate waveguides[J]. *Opt. Lett.* **47**, 1574-1577 (2022).
19. Y. Zhang, H. Li, T. Ding, Y. Huang, L. Liang, X. Sun, Y. Tang, J. Wang, S. Liu, Y. Zheng, and X. Chen. Scalable, fiber-compatible lithium-niobate-on-insulator micro-waveguides for efficient nonlinear photonics[J]. *Optica*, **10**, 688-693 (2023).
20. G. Li, Y. Chen, H. Jiang, and X. Chen. Broadband sum-frequency generation using d_{33} in periodically poled LiNbO₃ thin film in the telecommunications band[J]. *Opt. Lett.*, **42**, 939-942 (2017).
21. C. Wang, C. Langrock, A. Marandi, M. Jankowski, M. Zhang, B. Desiatov, M. M. Fejer, and M. Lončar. Ultrahigh-efficiency wavelength conversion in nanophotonic periodically poled lithium niobate waveguides[J]. *Optica* **5**, 1438-1441 (2018).
22. X. Li, H. Li, Z. Wang, Z. Chen, F. Ma, K. Zhang, W. Sun, and C. Wang. Advancing large-scale thin-film PPLN nonlinear photonics with segmented tunable micro-heaters[J]. *Photon. Res.* **12**, 1703-1708 (2024).
23. P.-K. Chen, I. Briggs, C. Cui, L. Zhang, M. Shah, and L. Fan. Adapted poling to break the nonlinear efficiency limit in nanophotonic lithium niobate waveguides[J]. *Nat. Nanotechnol.* **19**, 44-50 (2024).
24. Y. Su, X. Zhang, H. Chen, S. Li, J. Ma, W. Li, Y. Niu, Q. Qin, S. Yang, Y. Deng, Y. Zhang, X. Hu, and S. Zhu. High-efficiency nonlinear frequency conversion enabled by optimizing the ferroelectric domain structure in x-cut LNOI ridge waveguide[J]. *Nanophotonics*, **13**, 3477-3484 (2024).
25. B. Mu, X. Wu, Y. Niu, Y. Chen, X. Cai, Y. Gong, Z. Xie, X. Hu, and S. Zhu. Locally periodically poled LNOI ridge waveguide for second harmonic generation [J]. *Chin. Opt. Lett.*, **19**, 060007 (2021).
26. A. Rao, K. Abdelsalam, T. Sjaardema, A. Honardoost, GF Camacho-Gonzalez, and S. Fathpour. Actively-monitored periodic-poling in thin-film lithium niobate photonic waveguides with ultrahigh nonlinear conversion efficiency of $4600\%W^{-1}cm^{-2}$ [J]. *Opt. Express* **27**, 25920 (2019).
27. R. Wu, M. Wang, J. Xu, J. Qi, W. Chu, Z. Fang, J. Zhang, J. Zhou, L. Qiao, Z. Chai, J. Lin, and Y. Cheng. Long Low-Loss-Litium Niobate on Insulator Waveguides with Sub-Nanometer Surface Roughness[J]. *Nanomaterials*, **8**, 910 (2018).
28. J. Chen, Z. Liu, L. Song, C. Sun, G. Wang, and Y. Cheng. Ultra-high-speed high-resolution laser lithography for lithium niobate integrated photonics[C]. *Frontiers in Ultrafast Optics: Biomedical, Scientific, and Industrial Applications XXIII. SPIE*, 2023, 12411: 41-50.